atoms

MDPI

Article

Interferometry in an Atomic Fountain with Ytterbium Bose–Einstein Condensates

Daniel Gochnauer, Tahiyat Rahman, Anna Wirth-Singh and Subhadeep Gupta *

Department of Physics, University of Washington, Seattle, WA 98195, USA; thegochnauer@gmail.com (D.G.); tahiyatr@uw.edu (T.R.); annaw77@uw.edu (A.W.-S.)
* Correspondence: deepg@uw.edu

Abstract: We present enabling experimental tools and atom interferometer implementations in a vertical "fountain" geometry with ytterbium Bose–Einstein condensates. To meet the unique challenge of the heavy, non-magnetic atom, we apply a shaped optical potential to balance against gravity following evaporative cooling and demonstrate a double Mach–Zehnder interferometer suitable for applications such as gravity gradient measurements. Furthermore, we also investigate the use of a pulsed optical potential to act as a matter wave lens in the vertical direction during expansion of the Bose–Einstein condensate. This method is shown to be even more effective than the aforementioned shaped optical potential. The application of this method results in a reduction of velocity spread (or equivalently an increase in source brightness) of more than a factor of five, which we demonstrate using a two-pulse momentum-space Ramsey interferometer. The vertical geometry implementation of our diffraction beams ensures that the atomic center of mass maintains overlap with the pulsed atom optical elements, thus allowing extension of atom interferometer times beyond what is possible in a horizontal geometry. Our results thus provide useful tools for enhancing the precision of atom interferometry with ultracold ytterbium atoms.

Keywords: atom interferometry; Bose–Einstein condensate; quantum sensing

Citation: Gochnauer, D.; Rahman, T.; Wirth-Singh, A.; Gupta, S. Interferometry in an Atomic Fountain with Ytterbium Bose–Einstein Condensates. *Atoms* **2021**, *9*, 58. https://doi.org/10.3390/atoms9030058

Academic Editor: Andrea Bertoldi

Received: 12 July 2021
Accepted: 20 August 2021
Published: 25 August 2021

1. Introduction

Pulsed optical lattices are crucial tools for high precision atom interferometry (AI), with applications ranging from tests of fundamental physics to force sensing [1–5]. AI in free space rather than in a trapped geometry has the inherent advantage of not being susceptible to systematic effects from the confining potentials. Terrestrial pulsed-lattice atom interferometers have relied on a vertical geometry of diffraction beams in order to fully realize the inherent power of the method, as the loss of spatial overlap with the pulsed lattice from atoms falling due to gravity is suppressed in this configuration.

While laser cooled atoms have found pronounced success as sources for precision AI, a Bose–Einstein condensate (BEC) source offers improvement with an inherently narrow velocity distribution, which increases the coherence length and allows for longer interferometer times due to the slow spread of the atomic spatial distribution during free expansion. Spin-singlet ground state atoms, such as Sr and Yb, are particularly appealing for AI because of their near-insensitivity to external magnetic fields and the availability of several narrow optical transitions [2,6,7]. Furthermore, the heavy nucleus of the Yb atom supports the stability of multiple isotopes allowing for systematic cross-checks within the same apparatus as well as the possibility to perform AI with degenerate Bose or Fermi gases.

Prior work with Yb BEC atom interferometers [6,8–10] have all been restricted to geometries with horizontally oriented laser beams as the atom-optic elements. Adapting to a vertical geometry poses significant challenges due to the larger velocity spread in the vertical direction for BECs expanding out of typical atom traps. In this paper, we investigate solutions to these challenges using two separate methods of atom manipulation

via light shifts from laser beams shaped in position and in time. Using these methods, we successfully demonstrate AI with Yb BECs in a vertically oriented atomic fountain geometry and establish tools for future enhancement of AI precision.

The rest of this paper is organized as follows. In Section 2, we describe the production of our BEC source and the vertical fountain launch which prepares the atoms for interferometry. In Section 3, we present a gravity compensation beam method for reducing vertical velocity spread. With this method in place, we report on the first vertical Yb interferometer, performed in a double Mach–Zehnder configuration, in Section 4. Finally, in Section 5, we implement delta-kick collimation as an alternative method to the gravity compensation beam, and we demonstrate effectiveness of the technique through coherence length measurements using momentum-space Ramsey interferometry.

2. Yb BEC Fountain

We first briefly describe Yb BEC production in our apparatus [8,11] and then present the launch process which initiates the atomic fountain.

2.1. BEC Source and Atom Optics

Each of the experiments reported in this work begins with a trapping and cooling sequence for the production of a ytterbium (^{174}Yb) Bose–Einstein condensate consisting of 10^5 atoms [11]. A Yb atomic beam emerging from an effusive oven is slowed in a first stage through an increasing-field Zeeman slower and in a second stage using a pair of crossed laser beams [12]. The slowed atoms are then captured in a magneto-optic trap (MOT). The broad ($\Gamma_b = 2\pi \times 29$ MHz) dipole transition ($^1S_0 \rightarrow {}^1P_1$) at $\lambda_b = 399$ nm is used to slow the atoms, while the narrow ($\Gamma_g = 2\pi \times 182$ kHz) intercombination transition ($^1S_0 \rightarrow {}^3P_1$) at $\lambda_g = 556$ nm is used for the MOT trapping beams (see Figure 1a).

Following cooling in the MOT, atoms are transferred into a crossed optical dipole trap (ODT) for evaporative cooling towards BEC. The ODT is formed by a pair of 532 nm beams: one oriented horizontally, defining the x-axis, and the other nearly along the vertical y-axis. The evaporative cooling stage concludes with a BEC of 10^5 atoms in harmonic confinement characterized by trap frequencies $\omega_{x,y,z} = 2\pi \times (16, 200, 80)$ Hz. Subsequently, the BEC is released by suddenly switching off the ODT before the application of atom optics pulses. We note that the tightest confinement direction in the ODT is along the vertical axis, in order to counter the gravitational force on the heavy atom. A consequence of this general characteristic of optically trapped Yb is that the expansion of the BEC after release is mostly along the vertical, as most of the initial chemical potential is converted to kinetic energy in this direction [13,14], a quantity we measure to be $k_B \times (42 \pm 5)$ nK through absorption imaging after long expansion times.

The optical lattice used for the vertical fountain launch and the interferometer optics has a waist of 1.8 mm and is composed of a pair of vertically-oriented counter-propagating laser beams that are aligned to the atoms and controlled by independent acousto-optic modulators (AOMs). The optical frequency of the lattice is detuned from the $^1S_0 \rightarrow {}^3P_1$ transition by Δ and the frequency difference between the two lattice laser beams is δ (see Figure 1a and inset to Figure 1b). For the work presented here, Δ is set to $+3500\Gamma_g$ ($2\pi \times 637$ MHz), except in Section 5, where $\Delta = -3500\Gamma_g$. In general, the positive detuning leads to lower spontaneous scattering rates in the lattice. However, for either sign, the spontaneous scattering rate is less than 1 Hz in this work and negligible, even for the highest lattice depths used. For the experiments in Section 5, we choose the negative detuning to more easily allow generation of the attractive pulsed optical potential for delta-kick collimation using the same 556 nm laser source. The case where $\Delta = +3500\Gamma_g$ is depicted in Figure 1a. The quantity δ is always less than $2\pi \times 1$ MHz and varied with sub-Hz precision using direct digital synthesis radio-frequency sources that drive the lattice AOMs.

We note that the measured kinetic energy in the vertical direction corresponds to a velocity spread of $\Delta v \simeq 0.5 v_{\mathrm{rec}}$, where $v_{\mathrm{rec}} = \hbar k_g / m$ is the recoil velocity with $k_g = 2\pi/\lambda_g$ and m is the mass of a Yb atom. Since the coherence time relevant for signal-to-noise in

atom interferometry typically scales with $1/\Delta v$, it is important to address the reduction of this value, and much of the present work demonstrates successful techniques towards this end for Yb BEC vertical interferometers.

2.2. Vertical Fountain Launch

The vertical launch is performed by using Bloch oscillations for large momentum transfer. Such processes were carried out in the following sequence: (i) adiabatically turning on the optical lattice in the frame of the falling atoms, (ii) chirping the relative frequency difference of the lattice beams, δ, to accelerate the atoms, and (iii) adiabatically turning off the lattice once the desired atom velocity had been reached. During lattice turn-on and turn-off, an additional chirp of $\dot{\delta} = 2gk_g$ was necessary to maintain an inertial frame. Here, g is the acceleration due to gravity. The frequency sweep during the acceleration step was uniquely chosen for each set of experiments to optimize momentum transfer efficiency. A representative fountain launch is shown in Figure 1b.

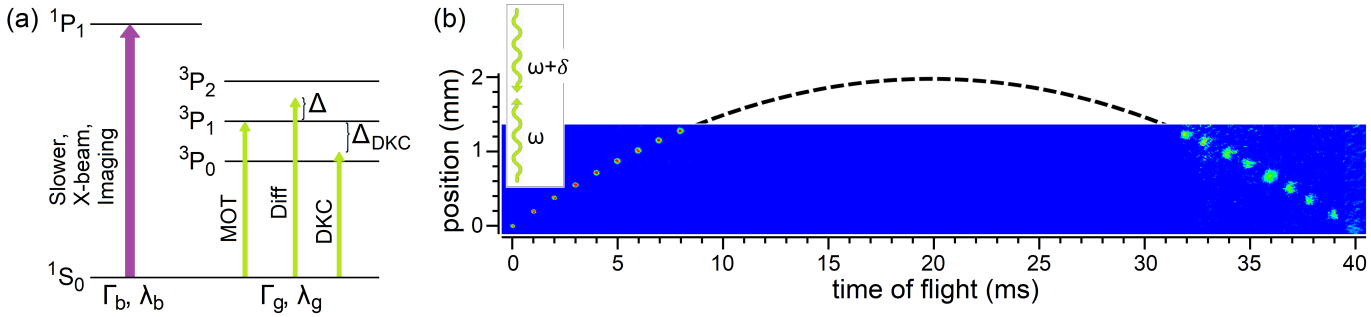

Figure 1. (**a**) Energy level diagram for ytterbium showing the optical transitions used in the experiment; (**b**) demonstration of a vertical fountain launch with 30 ground-band Bloch oscillations. The relative frequency sweep of the lattice beams was $\dot{\delta} = 2\pi \times 600$ kHz/ms. Time-of-flight absorption images show the trajectory of the atom cloud at variable times following the launch. The dashed line indicates the part of the trajectory that is out of view of the absorption imaging setup.

3. Gravity Compensation by Shaped Optical Beam

Atoms trapped in our ODT experience a potential proportional to the shape of the ODT beams as well as gravity. Due to the linear gravitational potential, there is a nonzero minimum allowable depth of the ODT such that it remains a trapping potential. This value increases as the vertical width of the horizontal ODT beam increases, resulting in a conflict between desires for both low trap frequency and low trap depth. This constraint can be lifted, however, by compensating the gravitational potential with an appropriately tuned linear optical potential in the trapping region [15]. Importantly, this technique is accessible for all atoms, including non-magnetic atoms such as ytterbium. Using a time-averaging technique discussed below, we implemented an appropriately shaped optical potential U_S to weaken the confinement along the vertical direction and thus the vertical kinetic energy during expansion after release from ODT. Assuming a Gaussian shape of the trapping beam (waist w_0), we can write the total potential seen by the atoms as

$$U(y) = U_0 e^{-2y^2/w_0^2} - mgy + U_S(y) \quad (1)$$

$$\simeq U_0\left(1 - \frac{2y^2}{w_0^2}\right) + (\alpha - mg)y = U_0 + \frac{1}{2}m\omega_y^2 y^2 + (\alpha - mg)y \quad (2)$$

where $U_0 (< 0)$ is the peak ODT Stark shift, w_0 is the ODT beam waist, $U_S(y)$ is the additional gravity compensation potential with $\alpha = \partial U_S/\partial y|_{y=0}$, and we have kept lowest order terms around $y = 0$ for Equation (2). U_S is tuned such that $\alpha \simeq mg$ at the location of the atoms.

The shaped beam used the same 532 nm light used for optical trapping. It was aligned to co-propagate with the horizontal ODT beam and—by means of an AOM—could be spatially modulated along the vertical axis (see Figure 2). We designed the input waveform

of the AOM such that the resultant time-averaged optical potential at the atoms would be linear over a region h, slightly larger than the trapping region. The function $\xi(t) = h\sqrt{\frac{\omega_p}{\pi}t}$ represents one half-period of this waveform and is therefore defined over $0 \leq t < \pi$ with a full oscillation frequency, ω_p. For this work, $\omega_p = 2\pi \times 4$ kHz, chosen to be much greater than the trap frequencies and less than the bandwidth of our electronics.

The gradient of this optical potential was adjusted by changing the total power in the beam while maintaining a constant time-averaged beam intensity profile. This would alter the gradient of the net background potential in the trapping region (see Figure 2a), resulting in a displacement to the local minimum of the ODT. When this shift is zero, the linear optical potential is assumed to be properly compensating gravity. Thus, we first determined the "zero point" location by measuring the position of the atom cloud as a function of ODT depth in the absence of the new shaped optical beam. The best-fit curve for the data shown in Figure 3a is a simple reciprocal function ($\propto 1/$ODT power), derived from a harmonic approximation valid near the center of the Gaussian ODT intensity profile (see Equation (2)). The convergent location observed at large ODT powers, corresponding to trap depths much higher than the gravitational potential variation across the trap, provided a benchmark value against which we could discern the effectiveness of the linear optical potential. The value is also marked in Figure 3b by the dashed line.

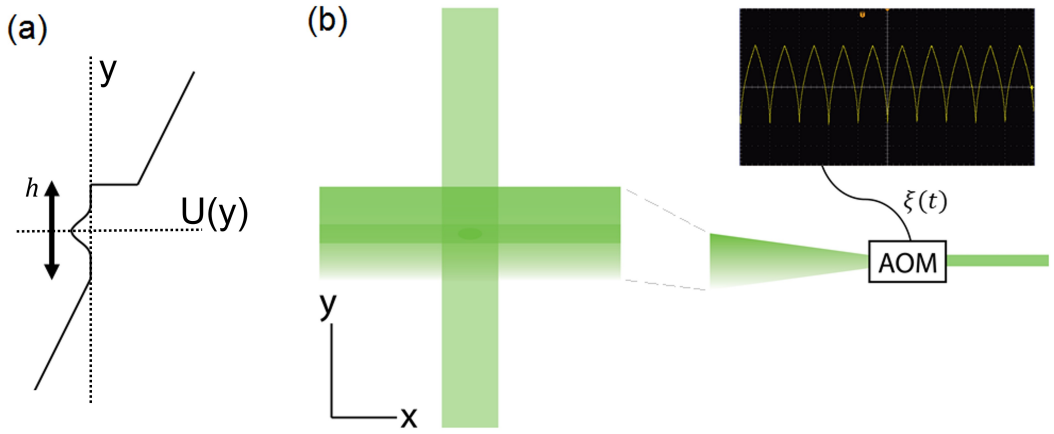

Figure 2. Implementation of a shaped optical beam for gravity compensation. (**a**) model for total optical potential along the vertical axis, through the center of the optical trapping region; (**b**) illustration of the ODT geometry along with the shaped optical beam. This beam is used to compensate the linear gravitational potential through use of an acousto-optic modulator supplied with the waveform, $\xi(t)$, as shown.

With the ODT returned to low depth (i.e., standard evaporation endpoint), we increased the total power in the shaped beam potential until the shift in the atoms' location was consistent with zero. This can be seen in Figure 3b where the two lines cross. The best-fit curve for the data in this figure is a line, again as a result of approximating a harmonic trapping potential near the center of the ODT (see Equation (2)). The optimal beam power from this procedure is then determined to be about 300 mW. Following this optimization, we used time-of-flight absorption imaging to measure the kinetic energy in the vertical direction to be $k_B \times (17 \pm 2)$ nK, a $42/17 \simeq 2.5$-fold improvement compared to without the gravity compensation beam. In terms of velocity spread, the reduction factor is $\sqrt{2.5} \simeq 1.6$.

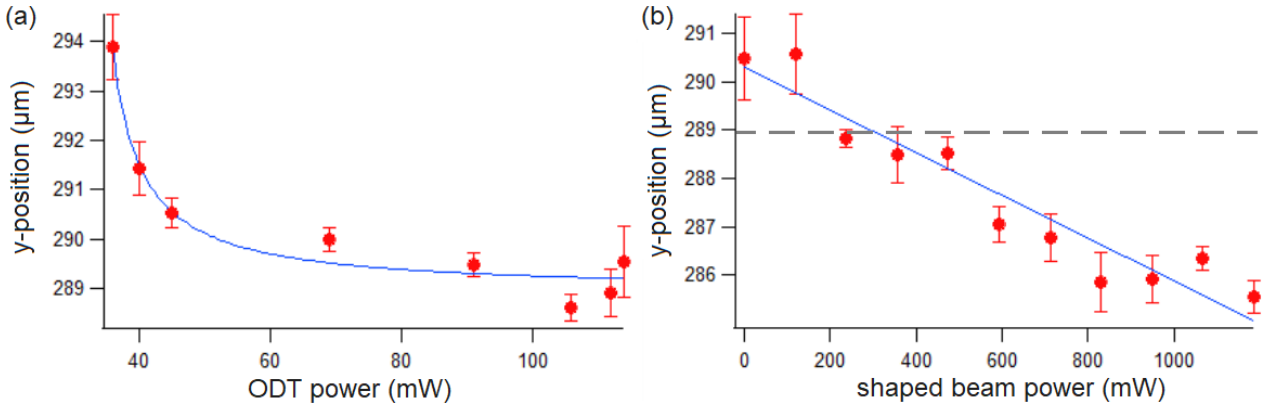

Figure 3. Optimization procedure for gravity compensation with a shaped optical beam. (**a**) measured BEC position with absorption imaging, as the ODT depth is increased. The converging locations at higher depths indicate a reduction of the displacement due to the gravitational potential. The blue curve is a best-fit reciprocal function; (**b**) introduction of the linear optical potential at low ODT depth. The BEC position has a nearly linear dependence on the shaped beam power as the net background potential gradient changes. The dashed line marks the asymptotic value of the reciprocal function shown in (**a**). The solid blue curve is a best-fit line to this data.

4. Double Mach–Zehnder Interferometer

We next report a demonstration of the first vertical Yb BEC interferometer. The geometry we use for this is a double Mach–Zehnder configuration, a design which is beneficial for precision measurement and sensing, since it suppresses vibration noise. In particular, the vertical double Mach–Zehnder interferometer is well-suited for gravity gradiometry applications [16].

Our implementation consists of four atom-optic elements: two splitting pulses, a mirror pulse, and a readout pulse. Each was implemented as a third-order Bragg pulse [9,17] with Gaussian $1/e$ full-width 54 μs in our vertical optical lattice with single-photon detuning, $\Delta = +3500\Gamma$. The typical peak lattice depth for a mirror pulse was $26\hbar\omega_{\mathrm{rec}}$ to satisfy the Bragg π–pulse condition, while the splitting and readout pulses had a peak depth of $14\hbar\omega_{\mathrm{rec}}$ and operated as $\pi/2$–pulses. Here, $\omega_{\mathrm{rec}} = \hbar k_g^2/2m$ is the recoil frequency. The relative detuning of the lattice beams was chirped at the rate $\dot{\delta} = 2gk_g$ for all pulses to account for the continuous Doppler shift of the falling atoms.

The double Mach–Zehnder interferometer geometry is depicted in Figure 4a in the accelerating frame of a falling atom cloud. To improve the efficiency of the momentum transfer within the interferometer, we apply an initial third-order Bragg π–pulse (not shown) to further narrow the width of the vertical velocity distribution. The two splitting pulses at the beginning of the interferometer are separated by a time Δt, which establishes the baseline between the two Mach–Zehnder interferometers. We chose Δt = 3 ms, which also made the interferometer paths visually distinguishable in our absorption images. From these images, we determine the relative populations in the output ports and observe interference fringes for each sub-interferometer, A and B (see Figure 4b). For long interferometer duration, however, physical vibrations affect an unknowable shift to the lattice phase, resulting in a reduction of fringe visibility for each sub-interferometer. Nonetheless, the differential interferometer phase for a double Mach–Zehnder, $\Delta\Phi = \Delta\phi_B - \Delta\phi_A$, is insensitive to vibration effects, which cancel out as a common mode phase shift. On the other hand, a finite differential phase can be generated from external forces such as a gravity gradient. This phase $\Delta\Phi$ can be observed by analyzing the correlation of sub-interferometer populations. As shown in Figure 4b, the fractional population in an output port of one sub-interferometer when plotted against that in an output port of the other sub-interferometer traces out an ellipse whose eccentricity determines $\Delta\Phi$ [18–21].

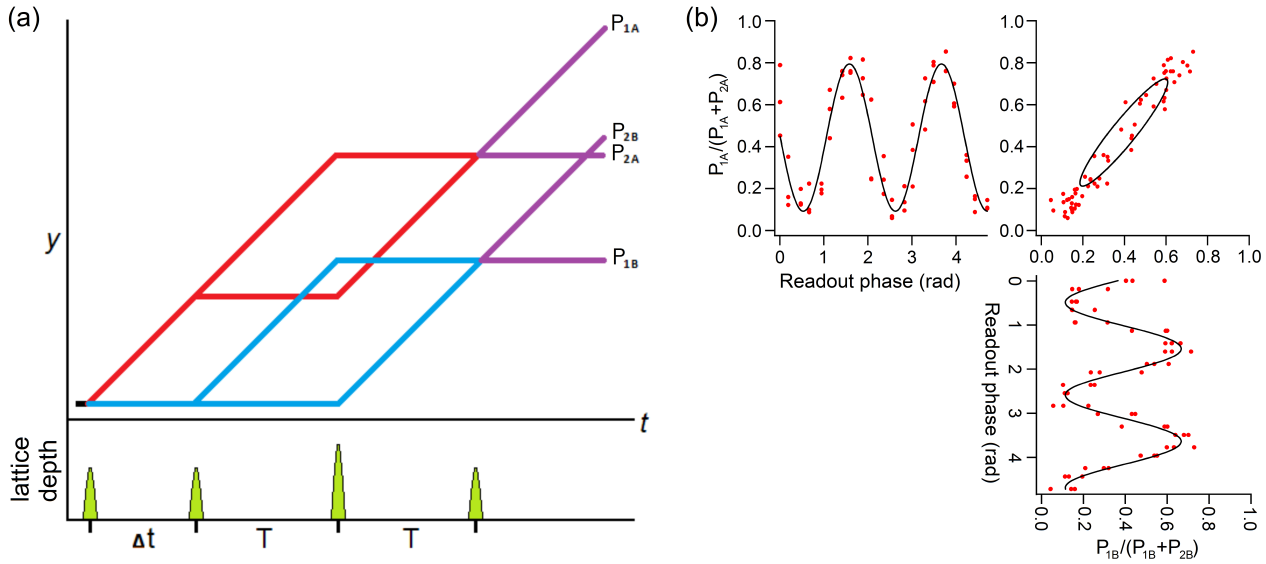

Figure 4. Double Mach–Zehnder interferometry. (**a**) Upper: Space-time diagram for a typical interferometer sequence shown in the accelerating frame of the free-falling BEC source such that the action of gravity is removed. The horizontal lines and the lines with finite slope correspond to interferometer paths separated in momentum by $6\hbar k_g$. Lower: Corresponding lattice pulse sequence; (**b**) representative ellipse signal for a double Mach–Zehnder interferometer with $\Delta t = 3$ ms and $T = 0.25$ ms. The oscillating populations in the output ports are plotted versus the phase of the readout lattice for the two sub-interferometers, from which an ellipse can be observed in the correlation of the populations in the top right parametric plot. All black curves are best fit sinusoids or ellipses.

To demonstrate robustness against vibrations, we extended the free evolution time within the interferometer, T, to values above the timescale of vibrations, which exist in our system at a bandwidth below 1 kHz. In this set of experiments, $T = 0.25$ ms, 1.25 ms, and 2.25 ms, covering nearly one whole order of magnitude. The visibility at short times is as high as 80% (see for $T = 0.25$ ms in Figure 4b), but drops with increasing T, and is consistent with zero by $T = 2.25$ ms. However, the ellipse traced out by the correlated populations is only marginally disturbed as shown in Figure 5. The fits (black curves in Figure 5) are obtained by first converting the data into polar coordinates, then performing a least-squares regression analysis using the function

$$r = \frac{a(1-e^2)}{1+e\cos(\theta-\theta_0)} \tag{3}$$

for an ellipse with one focus at the origin. In addition to the origin location, the given fit parameters describe the eccentricity of the ellipse, e, the length of the semi-major axis, a, and the rotation angle, θ_0. The differential interferometer phase can be determined from the eccentricity by the relation [18]

$$\Delta\Phi = \cos^{-1}\left(\frac{e^2}{2-e^2}\right) \tag{4}$$

which is defined over a one-quarter period.

The values of eccentricity returned by the fits are very close to 1, implying a differential phase close to zero. Indeed, the gravitational gradient for these parameters is expected to be negligibly small. The $\Delta\Phi$ corresponding to the measured $e \simeq 0.99$ is a few hundred mrad and may be due to atomic interactions. The calculated interaction energy for 3 ms expansion time and immediately before the first splitting $\pi/2$ pulse is 1.2 kHz. For a 10% level difference in arm splitting this gives rise to a few hundred mrad phase shift over the few millisecond timescale of the interferometer. This hypothesis is also consistent with the location of the center position of the ellipse deviating from the symmetric (0.5, 0.5) location at the 10% level. This deviation is a manifestation of deviations at the same level from

the $\pi/2$ condition for splitting pulses, and was independently verified by observing the correlation of the output port populations in the absence of the readout pulse. Further tuning of the $\pi/2$ pulses and longer expansion time to reduce the interaction strength, as is needed to scale-up the interferometer to larger times and enclosed areas, will make this differential phase contribution negligible. The deviation at the 10% level from $\pi/2$ pulses is also an important reason for the visibility of the sub-interferometers being less than 100% even at the shortest time T (see Figure 4b). We expect that unit visibility is approached (for T approaching zero) with better tuned $\pi/2$ and π pulses, as can be done by observing single-pulse Rabi oscillations (see, for e.g., [9]).

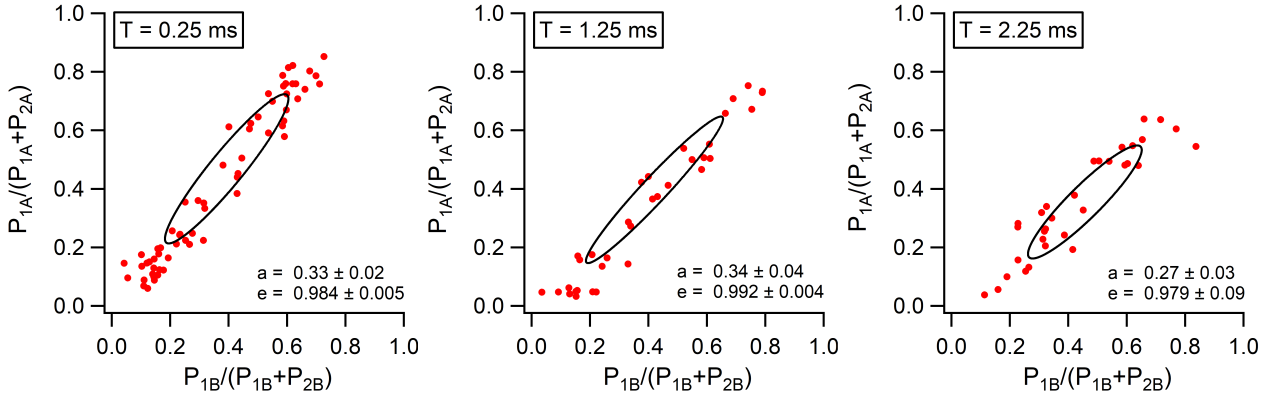

Figure 5. Ellipse signals at various values of T for a double Mach–Zehnder interferometer. Black curves are best fit ellipses for each data set. These are characterized by e, the eccentricity of the ellipse, and, a, the length of the semi-major axis.

Further development of our double Mach–Zehnder interferometer will involve methods to accurately calibrate the differential phase extraction procedure by applying large independently-known differential phases. While the use of magnetic pulses with associated Zeeman shifts works well for this purpose with alkali atoms [18], their use in spin-singlet atoms like ^{174}Yb is precluded by the lack of magnetic sensitivity. Instead, appropriately timed optical pulses with the associated AC Stark shifts can be used for this purpose.

5. Delta-Kick Collimation of Yb for Vertical AI

5.1. Delta-Kick Collimation

We now report on another technique to reduce the vertical velocity spread for Yb—delta-kick collimation (DKC)—which shows even better performance than the gravity compensation beam technique described earlier. This technique, also known as matter–wave lensing [22–24], has previously been demonstrated in alkali atoms, but not in spin-singlet atoms to the best of our knowledge. The process involves pulsing a parabolic attractive potential which may slow—or even halt—the expansion of the atom cloud in the corresponding dimension. In our system, this is applied as a pulsed optical potential at a time t_o after the BEC had been released from the ODT. The potential is derived from our 556 nm laser with a detuning, $\Delta_{\mathrm{DKC}} = -4600\Gamma$, red-shifted from the $^1S_0 \rightarrow {}^3P_1$ resonance. The DKC beam has a power of $\simeq$ 22 mW and is oriented horizontally, close to the horizontal ODT axis. It is focused with a waist size of $\simeq$ 150 µm at the location of the atoms. The DKC beam creates a transverse attractive potential for the atoms proportional to the Gaussian shape of the beam, which is parabolic to lowest order near the beam center with effective harmonic angular frequency ω_{DKC}.

To minimize the variance of the BEC position over the duration of the DKC pulse, δt, the pulse was applied at the apex of the atoms' trajectory following a vertical fountain launch. To facilitate beam alignment, the launch was designed to place the apex at the location of the trapped BEC (see Figure 6a). The optical lattice had a depth of about $30\hbar\omega_{\mathrm{rec}}$ during the launch and a single-photon detuning $\Delta = -3500\Gamma$. For a typical experiment, the launch consisted of 30 Bloch oscillations affected by chirping the relative lattice detuning at a rate of 500 kHz/ms. With these launch parameters, the time for the atoms to reach the

apex occurs $t_o = 25.4$ ms after release from the ODT. For an optimal delta-kick, we must simultaneously satisfy a thin lens criterion, $\delta t \ll t_o$, as well as the collimation condition, $\delta t \simeq 1/(\omega_{\mathrm{DKC}}^2 t_o)$.

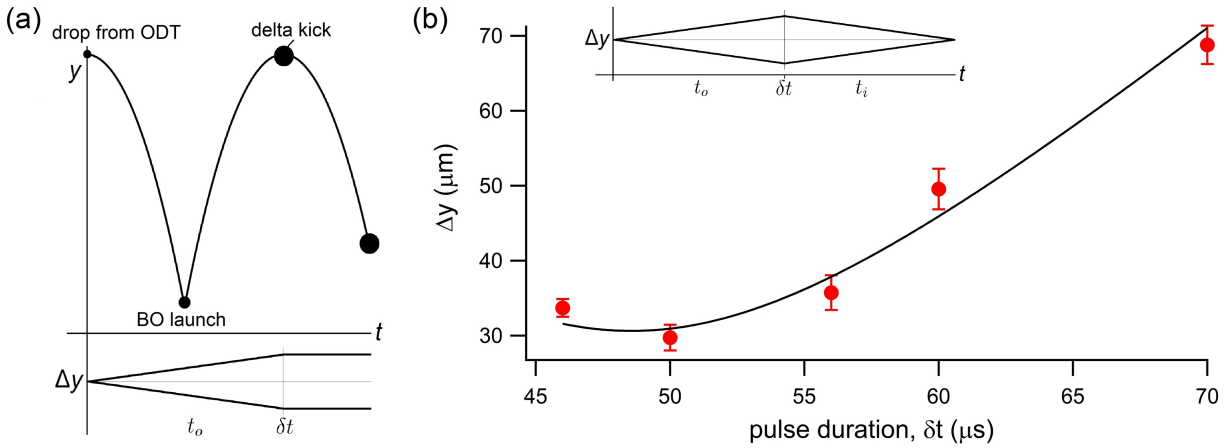

Figure 6. Delta-kick collimation and characterization sequences. (**a**) space-time diagram depicting the trajectory of the expanding atom cloud. The DKC pulse of duration δt is applied at time t_o after release from the ODT to achieve collimation; (**b**) DKC characterization by measuring the size of a refocused atom cloud at time t_i after the delta-kick. The black curve is a best-fit hyperbola, $(\Delta y)^2/(\Delta y_{\mathrm{min}})^2 - (\delta t - \delta t_{\mathrm{min}})^2/C^2 = 1$, returning a minimum observable size $\Delta y_{\mathrm{min}} = 30.6 \pm 2.0$ μm with a corresponding δt_{min} of 48.6 ± 1.9 μs. The DKC beam power here is approximately 22 mW.

We determined the capability of this collimation technique in our system from a characterization of our delta-kick lens and its effect on our atom source [23]. For this experimental sequence, we applied the delta-kick at time t_o, tuned to refocus the atom cloud at time t_i after the pulse, producing an image of the original object (BEC). By varying the pulse duration, we ascertained a minimum observable spot size, $\Delta y_{\mathrm{min}} = 30.6 \pm 2.0$ μm, in the vertical dimension. Under collimation conditions, our system should have an upper bound on the minimum spread in the velocity distribution according to $\Delta v_{\mathrm{bound}} = \Delta y_{\mathrm{min}}/t_i$, where Δv is the RMS velocity of the atoms after application of the lens. We can recast this as an upper bound on the minimum attainable spread of kinetic energy $m(\Delta v_{\mathrm{bound}})^2/2$ in the vertical direction. From our measurement (see Figure 6b) and within the given experimental parameters, we determined the upper bound for this value to be $k_B \times (2.0 \pm 0.25)$ nK for our system.

5.2. Ramsey Interferometry and Coherence Time Measurements

As a secondary characterization of our DKC lens, we analyzed the coherence length of the condensate before and after the DKC pulse. We incorporated a momentum-space Ramsey interferometer [25] into the sequence, which consisted of two low-amplitude 4 μs square Kapitza–Dirac pulses separated by a time, T_{Ramsey}, as depicted in Figure 7a. The population of each momentum state was measured at long time of flight (i.e., enough time to spatially resolve the states) and oscillations were observed in the average fraction in the higher-momentum states, $(N_{+1} + N_{-1})/2N$. Here, N is the total atom number and $N_{\pm 1}$ is the atom number in the momentum state $\pm 2\hbar k$. Only at short times will there be observable fringes while the various wavefunction components retain sufficient spatial overlap. Thus, the envelope on these oscillations gives a Ramsey coherence time which is a measure of the coherence length of the atom source, with the two related through the velocity separation between the interfering states. Fitting the data to a sinusoid with the expected angular frequency $4\omega_{\mathrm{rec}}$ and an exponential envelope, we measure coherence times of 129 ± 18 μs and 23 ± 3 μs for sequences with and without delta-kick collimation, respectively. Since the coherence time scales with the inverse of the velocity spread, this indicates a reduction factor of $(129/23) \simeq 5.6$ in the vertical velocity spread. The reduction factor for kinetic energy in the vertical direction is then $(129/23)^2 \simeq 31$ below the previously mentioned

$k_B \times 42\,\mathrm{nK}$ value, i.e., $k_B \times 1.3\,\mathrm{nK}$. This is consistent with the upper bound on the kinetic energy $k_B \times 2\,\mathrm{nK}$, discussed in Section 5.1.

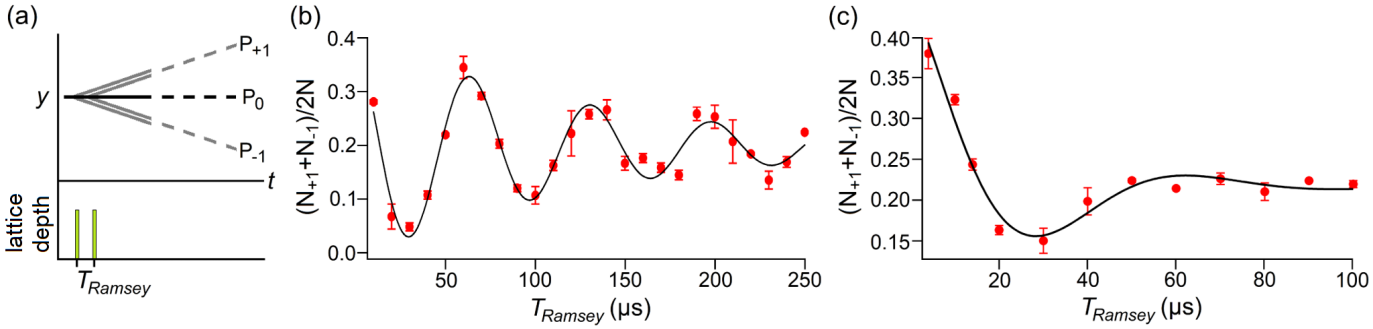

Figure 7. Characterization of DKC by coherence length measurements using Ramsey interferometry. (**a**) space-time diagram of a momentum-space Ramsey interferometer composed of two Kapitza-Dirac pulses. Decaying oscillations of population amplitude, with (**b**) and without (**c**) delta-kick collimation. The fit function, $f(t) = Ae^{-t/\tau}\sin(4\omega_{\mathrm{rec}}t + \phi) + f_0$, returns Ramsey coherence times of $\tau = 129 \pm 18$ μs and 23 ± 3 μs, respectively.

6. Conclusions

In summary, we have investigated two methods to reduce the vertical velocity spread of a Yb BEC and applied them towards atom interferometry in vertical fountain geometries. We developed a gravity compensation optical potential which reduced the vertical velocity spread by a factor of 1.6, and employed this gain towards demonstrating a vertical double Mach–Zehnder interferometer. The implementation of delta-kick collimation reduced the vertical velocity spread by a factor of 5.6, which we measured using a Ramsey interferometer technique in an atomic fountain setup. These first demonstrations of vertical AI with Yb BECs reported here are performed with fountain times in the tens of milliseconds, and we expect that the reduction of vertical velocity spread achieved here should greatly benefit extensions to longer fountain times of hundreds of milliseconds.

Taken together, our results provide useful manipulation tools for ultracold Yb, an important atom for applications in fundamental physics and next generation time standards [26,27], precision atom interferometry and sensing [6,8,28–30], quantum simulation [31–35], and quantum information science [36–38]. In particular, we expect the DKC methods to fruitfully impact future applications of Yb atom interferometers for precision sensing such as gravity gradiometry and tests of fundamental physics [5,30,39,40].

Author Contributions: Conceptualization, D.G. and S.G.; methodology, D.G., T.R., A.W.-S. and S.G.; software, D.G.; validation, D.G., T.R., A.W.-S. and S.G.; formal analysis, D.G., T.R., A.W.-S. and S.G.; investigation, D.G., T.R., A.W.-S. and S.G.; writing—original draft preparation, D.G. and S.G.; writing—review and editing, T.R. and A.W.-S.; visualization, D.G. and S.G.; supervision, S.G.; project administration, S.G.; funding acquisition, S.G. All authors have read and agreed to the published version of the manuscript.

Funding: This work was supported by the NSF Grant No. PHY-1707575.

Institutional Review Board Statement: Not applicable.

Informed Consent Statement: Not applicable.

Data Availability Statement: Available from the authors upon reasonable request.

Conflicts of Interest: The authors declare no conflict of interest.

References

1. Bouchendira, R.; Clade, P.; Guellati-Khelifa, S.; Nez, F.; Biraben, F. New Determination of the Fine Structure Constant and Test of the Quantum Electrodynamics. *Phys. Rev. Lett.* **2011**, *106*, 080801. [CrossRef]
2. Mazzoni, T.; Zhang, X.; Del Aguila, R.; Salvi, L.; Poli, N.; Tino, G. Large-momentum-transfer Bragg interferometer with strontium atoms. *Phys. Rev. A* **2015**, *92*, 053619. [CrossRef]

3. Hu, L.; Poli, N.; Salvi, L.; Tino, G. Atom Interferometry with the Sr Optical Clock Transition. *Phys. Rev. Lett.* **2017**, *119*, 263601. [CrossRef]
4. Parker, R.H.; Yu, C.; Estey, B.; Zhong, W.; Muller, H. Measurement of the fine-structure constant as a test of the Standard Model. *Science* **2018**, *360*, 191. [CrossRef] [PubMed]
5. Asenbaum, P.; Overstreet, C.; Kovachy, T.; Brown, D.; Hogan, J.; Kasevich, M. Phase Shift in an Atom Interferometer due to Spacetime Curvature across its Wave Function. *Phys. Rev. Lett.* **2017**, *118*, 183602. [CrossRef]
6. Jamison, A.O.; Plotkin-Swing, B.; Gupta, S. Advances in Precision Contrast Interferometry with Yb Bose–Einstein condensates. *Phys. Rev. A* **2014**, *90*, 063606. [CrossRef]
7. Rudolph, J.; Wilkason, T.; Nantel, M.; Swan, H.; Holland, C.; Jiang, Y.; Garber, B.; Carman, S.; Hogan, J. Large Momentum Transfer Clock Atom Interferometry on the 689 nm Intercombination Line of Strontium. *Phys. Rev. Lett.* **2020**, *124*, 083604. [CrossRef] [PubMed]
8. Plotkin-Swing, B.; Gochnauer, D.; McAlpine, K.; Cooper, E.; Jamison, A.; Gupta, S. Three-Path Atom Interferometry with Large Momentum Separation. *Phys. Rev. Lett.* **2018**, *121*, 133201. [CrossRef]
9. Gochnauer, D.; McAlpine, K.; Plotkin-Swing, B.; Jamison, A.; Gupta, S. Bloch-band picture for light-pulse atom diffraction and interferometry. *Phys. Rev. A.* **2019**, *100*, 043611. [CrossRef]
10. McAlpine, K.; Gochnauer, D.; Gupta, S. Excited-band Bloch oscillations for precision atom interferometry. *Phys. Rev. A.* **2020**, *101*, 023614. [CrossRef]
11. Plotkin-Swing, B. Large Momentum Separation Matter Wave Interferometry. Ph.D. Thesis, University of Washington, Seattle, WA, USA, 2018.
12. Plotkin-Swing, B.; Wirth, A.; Gochnauer, D.; Rahman, T.; McAlpine, K.; Gupta, S. Crossed-beam slowing to enhance narrow-line ytterbium magneto-optic traps. *Rev. Sci. Instrum.* **2020**, *91*, 093201. [CrossRef] [PubMed]
13. Castin, Y.; Dum, R. Bose–Einstein Condensates in Time Dependent Traps. *Phys. Rev. Lett.* **1996**, *77*, 5315. [CrossRef] [PubMed]
14. Jamison, A.O.; Kutz, J.N.; Gupta, S. Atomic Interactions in Precision Interferometry Using Bose–Einstein Condensates. *Phys. Rev. A.* **2011**, *84*, 043643. [CrossRef]
15. Shibata, K.; Ikeda, H.; Suzuki, R.; Hirano, T. Compensation of gravity on cold atoms by a linear optical potential. *Phys. Rev. Res.* **2020**, *2*, 013068. [CrossRef]
16. McGuirk, J.M.; Foster, G.T.; Fixler, J.B.; Snadden, M.J.; Kasevich, M.A. Sensitive absolute-gravity gradiometry using atom interferometry. *Phys. Rev. A* **2002**, *65*, 033608. [CrossRef]
17. Gupta, S.; Leanhardt, A.E.; Cronin, A.D.; Pritchard, D.E. Coherent Manipulation of Atoms with Standing Light Waves. *C. R. Acad. Sci. IV-Phys.* **2001**, *2*, 479. [CrossRef]
18. Foster, G.T.; Fixler, J.B.; McGuirk, J.M.; Kasevich, M.A. Method of phase extraction between coupled atom interferometers using ellipse-specific fitting. *Opt. Lett.* **2002**, *27*, 951. [CrossRef] [PubMed]
19. Stockton, J.K.; Wu, X.; Kasevich, M.A. Bayesian estimation of differential interferometer phase. *Phys. Rev. A* **2007**, *76*, 033613. [CrossRef]
20. Bertoldi, A.; Lamporesi, G.; Cacciapuoti, L.; de Angelis, M.; Fattori, M.; Petelski, T.; Peters, A.; Prevedelli, M.; Stuhler, J.; Tino, G. Atom interferometry gravity-gradiometer for the determination of the Newtonian gravitational constant G. *Eur. Phys. J. D* **2006**, *40*, 271–279. [CrossRef]
21. Chiow, S.; Herrmann, S.; Chu, S.; Muller, H. Noise-Immune Conjugate Large-Area Atom Interferometers. *Phys. Rev. Lett.* **2009**, *103*, 050402. [CrossRef]
22. Chu, S.; Bjorkholm, J.; Ashkin, A.; Gordon, J.; Hollberg, L. Proposal for optically cooling atoms to temperatures of the order of 10^{-6} K. *Opt. Lett.* **1986**, *11*, 73. [CrossRef] [PubMed]
23. Kovachy, T.; Hogan, J.; Sugarbaker, A.; Dickerson, S.; Donnelly, C.; Overstreet, C.; Kasevich, M. Matter Wave Lensing to Picokelvin Temperatures. *Phys. Rev. Lett.* **2015**, *114*, 143004. [CrossRef] [PubMed]
24. Muntinga, H.; Ahlers, H.; Krutzik, M.; Wenzlawski, A.; Arnold, S.; Becker, D.; Bongs, K.; Dittus, H.; Duncker, H.; Gaaloul, N.; et al. Interferometry with Bose–Einstein Condensates in Microgravity. *Phys. Rev. Lett.* **2013**, *110*, 093602. [CrossRef] [PubMed]
25. Hagley, E.W.; Deng, L.; Kozuma, M.; Trippenbach, M.; Band, Y.B.; Edwards, M.; Doery, M.; Julienne, P.S.; Helmerson, K.; Rolston, S.L.; et al. Measurement of the Coherence of a Bose–Einstein Condensate. *Phys. Rev. Lett.* **1999**, *83*, 3112. [CrossRef]
26. Dzuba, V.; Flambaum, V.; Schiller, S. Testing physics beyond the standard model through additional clock transitions in neutral ytterbium. *Phys. Rev. A* **2018**, *98*, 022501. [CrossRef]
27. Hinkley, N.; Sherman, J.; Phillips, N.; Schioppo, M.; Lemke, N.; Beloy, K.; Pizzocaro, M.; Oates, C.; Ludlow, A. An Atomic Clock With 10^{-18} Instability. *Science* **2013**, *341*, 1215–1218. [CrossRef]
28. Hartwig, J.; Abend, S.; Schubert, S.; Schlippert, D.; Ahlers, H.; Posso-Trujillo, K.; Gaaloul, N.; Ertmer, W.; Rasel, E. Testing the universality of free fall with rubidium and ytterbium in a very large baseline atom interferometer. *New J. Phys.* **2015**, *17*, 035011. [CrossRef]
29. Niederriter, R.; Schlupf, C.; Hamilton, P. Cavity probe for real-time detection of atom dynamics in an optical lattice. *Phys. Rev. A* **2020**, *102*, 051301(R). [CrossRef]
30. Roura, A.; Schubert, C.; Schlippert, D.; Rasel, E. Measuring gravitational time dilation with delocalized quantum superpositions. *arXiv* **2020**, arXiv:2010.11156.

31. Takasu, Y.; Maki, K.; Komori, K.; Takano, T.; Honda, K.; Kumakura, M.; Yabuzaki, T.; Takahashi, Y. Spin-singlet Bose–Einstein Condensation of Two-Electron Atoms. *Phys. Rev. Lett.* **2002**, *91*, 040404. [CrossRef]
32. See Toh, J.; McCormick, K.; Tang, X.; Su, Y.; Luo, X.; Zhang, C.; Gupta, S. Observation of Many-body Dynamical Delocalization in a Kicked Ultracold Gas. *arXiv* **2021**, arXiv:2106.13773.
33. Pagano, G.; Mancini, M.; Cappellini, G.; Lombardi, P.; Schäfer, F.; Hu, H.; Liu, X.; Catani, J.; Sias, C.; Inguscio, M.; et al. A one-dimensional liquid of fermions with tunable spin. *Nat. Phys.* **2014**, *10*, 198–201. [CrossRef]
34. Scazza, F.; Hofrichter, C.; Höfer, M.; De Groot, P.; Bloch, I.; Fölling, S. Observation of two-orbital spin-exchange interactions with ultracold SU(N)-symmetric fermions. *Nat. Phys.* **2014**, *10*, 779–784. [CrossRef]
35. Ono, K.; Kobayashi, J.; Amano, Y.; Sato, K.; Takahashi, Y. Antiferromagnetic interorbital spin-exchange interaction of ^{171}Yb. *Phys. Rev. A* **2019**, *99*, 032707. [CrossRef]
36. Stock, R.; Babcock, N.; Raizen, M.; Sanders, B. Entanglement of group-II-like atoms with fast measurement for quantum information processing. *Phys. Rev. A* **2008**, *78*, 022301. [CrossRef]
37. Saskin, S.; Wilson, J.; Grinkemeyer, B.; Thompson, J. Narrow-Line Cooling and Imaging of Ytterbium Atoms in an Optical Tweezer Array. *Phys. Rev. Lett.* **2019**, *122*, 143002. [CrossRef] [PubMed]
38. Covey, J.; Sipahigil, A.; Szoke, S.; Sinclair, N.; Endres, M.; Painter, O. Telecom-Band Quantum Optics with Ytterbium Atoms and Silicon Nanophotonics. *Phys. Rev. App.* **2019**, *11*, 034044. [CrossRef]
39. Schlippert, D.; Hartwig, J.; Albers, H.; Richardson, L.; Schubert, C.; Roura, A.; Schleich, W.; Ertmer, W.; Rasel, E. Quantum Test of the Universality of Free Fall. *Phys. Rev. Lett.* **2014**, *112*, 203002. [CrossRef]
40. Asenbaum, P.; Overstreet, C.; Kim, M.; Curti, J.; Kasevich, M. Atom-Interferometric Test of the Equivalence Principle at the 10^{-12} Level. *Phys. Rev. Lett.* **2020**, *125*, 191101. [CrossRef]